Reversible Cluster Aggregation and Growth Model for Graphene Suspensions

Michail Alifierakis [iD], **Kevin S. Sallah, and Ilhan A. Aksay**
Dept. of Chemical and Biological Engineering, Princeton University, Princeton, NJ 08544

Jean H. Prévost
Dept. of Civil and Environmental Engineering, Princeton University, Princeton, NJ 08544

We present a reversible cluster aggregation model for 2-D macromolecules represented by line segments in 2-D; and, we use it to describe the aggregation process of functionalized graphene particles in an aqueous SDS surfactant solution. The model produces clusters with similar sizes and structures as a function of SDS concentration in agreement with experiments and predicts the existence of a critical surfactant concentration (C_{crit}) beyond which thermodynamically stable graphene suspensions form. Around C_{crit}, particles form dense clusters rapidly and sediment. At $C \ll C_{crit}$, a contiguous ramified network of graphene gel forms which also densifies, but at a slower rate, and sediments with time. The deaggregation–reaggregation mechanism of our model captures the restructuring of the large aggregates towards a graphite-like structure for the low SDS concentrations. © 2017 American Institute of Chemical Engineers *AIChE J*, 63: 5462–5473, 2017
Keywords: graphene, aggregation, dispersion, Diffusion Limited Aggregation (DLA), Sodium Dodecyl Sulfate (SDS), water

Introduction

Graphene,[1] graphene oxide,[2,3] and reduced graphene oxides[4] as atomically thin macromolecular sheets are used in an increasing number of practical applications such as liquid fuels,[5] polymer composites,[6–8] energy storage and energy conversion devices (e.g., batteries, supercapacitors, solar cells),[9–18] and inks (for printed electronics and sensors).[19–21] In most of these applications, the molecular sheets have to be first dispersed in a liquid medium to break up powder aggregates and achieve the advantages of individual sheets. To do so, two prevalent colloidal dispersion methods are used: (1) decrease the magnitude of the van der Waals (vdW) attractive forces to the k_BT range (where k_B is the Boltzmann constant and T temperature) by lowering the Hamaker constant through index matching (which is also used as a method for graphite exfoliation);[22] or (2) counteract the vdW forces by inducing repulsion between the sheets through electrostatic, steric, or electrosteric interactions.[23,24] Ultimately, during the production of a device, the dispersed suspensions are converted to an aggregated state either through the stacking of graphene particles with themselves or with the colloidal particles of other phases. In such aggregated structures, a deterministic control of the topological features is of paramount importance to

define properties by controlling parameters such as accessible area for chemical reactions, load transfer for mechanical properties, electron and heat transfer for electronic and thermal properties. To this end, research efforts have been exclusively experimental to observe the effects of dispersion quality on the final properties of the products.[6,24–29]

However, while these experimental studies have been invaluable in many aspects, an accurate connection between the filler's network structure and the properties of the final materials has not been established. In theoretical modeling studies of the dependence of properties to particle dispersion, a well-defined topological state, spanning from the length scale of the atomically thin sheets, needs to be defined as input to a given model. If we could predict the relative position of the graphene particles, we could then aim at predicting the properties of the materials and yield a deeper understanding of the underlying mechanisms. This information is difficult to obtain by experimental methods. Even though individual graphene particles and aggregates of particles can be imaged through Scanning Electron Microscopy (SEM) or Transmission Electron Microscopy (TEM) techniques, the interpretation of those results can be difficult because of the low atomic number contrast between graphene and carbon-based polymers, the small thickness and wrinkled morphology of graphene sheets[8] and because of inherent difficulties in plate-like particle imaging (such as telling the difference between stacked and individual sheets, the natural variations in particle lengths, the anisotropy of their shapes etc.).[30]

In this article, we are focusing on a modeling approach to establish the dispersion state of the filler particles. This will

potentially provide a way of producing input for modeling studies of graphene-filled materials and a theoretical base to understand the important factors that affect the dispersion state of these particles. In addition, allowing for easy incorporation of flow in the suggested aggregation model can provide a tool that will allow better process control and design of processes that include atomically thin macromolecules. Similar to what has been done before for spherical and nonspherical particles.[31–33]

To that end, we present a reversible cluster aggregation and growth model for atomically thin macromolecules that predicts qualitatively the experimentally observed macroscopic colloidal aggregated structures.

As a case study, we focus on the prediction of aggregated structures experimentally observed with graphene-like materials although our model is not limited to graphene but is generic for any atomically thin molecular sheet. Based on the experiments[24] that we model, the length-scale of interest for this type of problem is in the order of nm in thickness and μm or tens of μm in the planar orientation of the molecular sheets. The time scales can vary from minutes to hours or even months.[24] These are significantly larger than the typical scales handled by molecular dynamics or even coarse-grained molecular dynamics,[34] Brownian dynamics,[35] and dissipative particle dynamics[36] simulations. A Stokesian dynamics simulation[37] would seem more appropriate in terms of length-scale but there are no reported efforts to model the dispersion behavior of a large number of graphene-like particles. Two possible reasons for this lack of literature on Stokesian dynamics are the difficulties of representing the accurate shape of graphene and of approximating the long-range interparticle forces. These problems are innate to modeling graphene particles at these length-scales.[38] Our approach is to simplify the geometry of the particles to rigid linear segments and to use a diffusion limited aggregation (DLA)-type of approach to simplify the force field and deal with the long-time scales of this problem. As we show in Results and Discussion section, these assumptions hinder our ability to obtain analytically quantitative results; but, they are sufficient for qualitative purposes.

The DLA model was introduced in 1981 by Witten and Sander[39] and it immediately spurred an immense interest in the field of colloidal-particle dispersion and aggregation. DLA is a lattice model that starts with a seed particle at the origin and new particles are added, one at a time, which perform random walks until they collide with the seed (i.e., the growing cluster) and become a part of it, or until they touch a boundary, in which case they are removed and a new particle is added. This leads to the formation of a cluster with a correlation exponent that can be related to experimental results for metal-particle aggregates.[39] This work gave rise to many similar models that tried to capture the physical reality of the aggregation process of different colloidal-particle systems, including the diffusion limited cluster aggregation (DLCA) model,[40,41] where particles as well as clusters of particles are allowed to diffuse in space; models with finite aggregation probability,[42–46] where collisions do not always lead to aggregation and can reach the reaction limited cluster aggregation (RLCA) limit as this probability tends to zero; and, the restructuring aggregation models, where clusters are allowed to reorganize with time either by the deaggregation of particles from the formed clusters (reversible aggregation)[47–58] or by reorganization of particles within the formed clusters.[59–63] The word "cluster" in this work (and consistent with the above literature)

indicates the product of a successful collision between (1) two particles, (2) a cluster and a particle, or (3) two clusters. The word "aggregation" is used to describe any event that leads to increase in cluster size.

Aggregate restructuring is a phenomenon that has been proven experimentally[64–69] and we consider it an important aspect of our approach, especially to model the recent experimental results of Hsieh et al. on the aggregation of graphene in aqueous surfactant solutions.[24] These results showed that there is restructuring of graphene aggregates leading to time dependent densification towards more compact structures over the time period of one year. The Shih-Aksay-Kikuchi (SAK) model[49] was the first reversible aggregation model to incorporate interaction potential in the calculation of the deaggregation probability of particles. The SAK is essentially a DLCA model that allows deaggregation of particles based on a deaggregation probability that is a function of the number of neighbors: fewer neighbors lead to higher probability of deaggregation. In this model, the particles are spherical and thus contact each other only at a point.

This approach is very attractive for our case because we aim to create a general Reversible Cluster Aggregation (RCA) growth model that can be used for systems with different interaction potentials (the difference in interaction potential caused by different surfactant concentrations as is expressed mathematically in the next section). But, as we aim to model atomically thin macromolecules that contact with each other at different points with variable contact angles and areas, in our case, the interaction potential will also depend on the contact area (comprised of contact angle and contact point) between the sheets. To allow rotation, we follow a nonlattice approach as opposed to the lattice approach of the SAK model and we also add an aggregation probability calculation, in addition to the deaggregation probability that is found in the SAK model, to make it more amenable to generalization. To the best of our knowledge, there is no work that deals with reversible aggregation of atomically thin macromolecules or sheets even though there are DLA-type models that deal with nonspherical particle shapes.[60,70–72]

The RCA model developed in this study is detailed in the following section. We test its validity by utilizing Hsieh et al.'s recent experimental results[24] on the aggregation of reduced graphene oxide sheets which we will refer to as functionalized graphene sheet (FGS) from here on. In the aforementioned work, FGSs were first dispersed in an aqueous sodium dodecyl sulfate (SDS) solution by ultrasonication at different adsorption levels of SDS.[24] Above a threshold SDS concentration of 10 μM (C_{crit}, where C is the SDS concentration) at 0.1 mg/mL FGS, suspensions stayed dispersed; while below that threshold concentration, aggregation and sedimentation were observed. Variations in the dispersion state were attributed to the adsorption of anionic dodecyl sulfate (DS$^-$) molecules onto FGSs that imparted varying levels of electrostatic repulsion between the sheets at different SDS concentrations. When dealing with the fully dispersible FGS, five basic types of structures were observed under optical microscopic characterization with varying SDS concentration as summarized in Figure 1 (adapted from Ref. 24): (1) a highly ramified network of aggregates (Figure 1a) that spans through the entire system (i.e., a gel-like state) when no SDS was added; (2) less-ramified aggregates (Figure 1b) at around $C = 5$ μM; (3) large compact aggregates (Figure 1c) of ~10 μm in size along with some micrometer size particles at around $C = 10$ μM; (4)
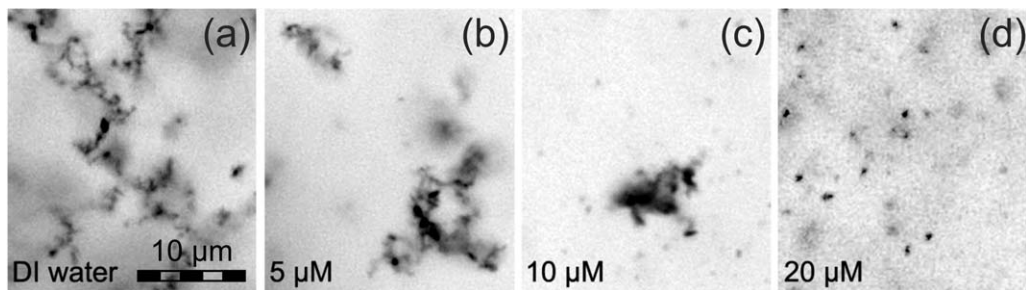
Figure 1. Representative optical microscope images of FGSs dispersed at a concentration of 0.1 mg/mL in aqueous SDS solutions after sonication.

SDS concentration in each suspension was: (a) 0 μM (DI water), (b) 5 μM, (c) 10 μM, (d) 20 μM. The scale bar is the same for all images. Adapted from Ref. 24.

dispersed single- or few-layer sheets (Figure 1d) at $C > 10$ μM, threshold concentration; and (5) hard aggregates of a few μm in size (Figure 1d) corresponding to partially oxidized graphite particles that do not fully disperse to single graphene oxide sheets. These observations display the effect of variable interaction potential between the FGSs as SDS adsorption on FGS changes.

However, the optical microscopic images of Figure 1 only display the state of the suspensions right after the dispersion of the suspensions by ultrasonication. When these suspensions are allowed to age up to one year, ultraviolet-visible (UV-Vis) light absorption of the supernatant indicates a significant amount of sedimentation below the threshold SDS concentration of 10 μM as shown in Figure 2 (adapted from Ref. 24). While the blue curve corresponds to images presented in Figure 1, the supernatants of the suspensions below 10 μM threshold concentration become highly transparent as aggregates settle out with aging time. This indicates that the aggregates of Figures 1a–c densify further with time. While these experiments do not provide a clear mechanism for the densification process, the RCA growth model we present in the following section suggests that at $C < C_{crit}$ the restructuring of the graphene aggregates is the cause of densification with time but there are kinetic reasons that limit the restructuring rate of the aggregates. The model also predicts a threshold surfactant concentration (C_{crit}) above which thermodynamically stable dispersed single or few-particle aggregates are observed as outlined with light gray shaded region in Figure 2.

Model and Application

Our RCA model is in principle a reversible aggregation model that explores the spectrum between DLCA and RLCA. The particles are represented in 2-D by line segments of unit length that are moving freely (off-lattice simulation) in a square matrix with periodic boundary conditions by performing translational and rotational steps. Imminent collisions between particles/clusters happen with a certain probability (which we will call aggregation probability) and produce clusters. Particles can detach themselves from the clusters that they are part of with a certain probability that we will call deaggregation probability.

We initially place the particles at random positions and random orientations in a square matrix, making sure that they do not overlap with each other, do not form clusters and do not touch the boundaries. At each time step, we pick one of the existing particles/clusters. Depending on the step, this particle/cluster is destined to perform either a rotation or a translation

(this option interchanges step by step). We decide the direction of the possible movement; and, based on an aggregation probability calculation, two particles/clusters that are sufficiently close to each other and are meant to collide will either collide and aggregate or will not move at all. At the end of each step, we pick a particle at random and if it belongs to a cluster then we decide whether it will deaggregate from all its neighbors or not based on a deaggregation probability calculation. A more detailed algorithm is provided in Supporting Information Appendix A and Figure S1.

The above description is based on the assumption that line segments in a 2-D matrix represent plate-like particles in 3-D.
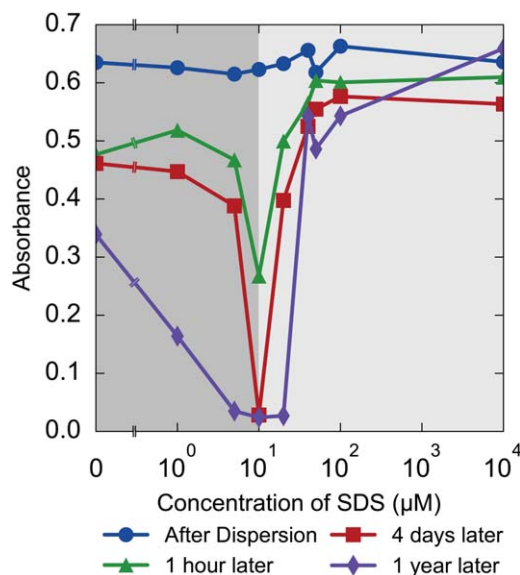

Figure 2. UV-Vis absorbance of suspensions with FGSs dispersed at a concentration of 0.1mg/mL, in SDS solutions with various SDS concentrations, a few minutes after sonication (blue line) as well as after the first centrifugation (1 h later, green line), and after centrifugation 4 days (red line) and 1 year (purple line) later; All samples were diluted 1:9 prior to absorbance measurements.

The dark gray region marks the surfactant concentration values for which an aggregated state is formed. The light gray region shows the surfactant concentrations for which the particles remain dispersed. The x-axis is logarithmic but the value of 0 was added on the left to help in a comparison with Figure 1. Adapted from Ref. 24. [Color figure can be viewed at wileyonlinelibrary.com]

If we imagine that there is a third-dimension perpendicular to the simulation space and our line segments extend in that space, then we can see our particles as 2-D plates that are all parallel to the axis that defines the third dimension and are restricted within the same boundaries with respect to that dimension (i.e., concentric). This is the basic assumption we make to reduce our model to 2-D. We assume no movement in the third dimension; but, we cannot ignore it entirely as our particles need to have a non-zero volume to use the electrostatic equations that we present below. Assuming they are concentric is a reasonable assumption that ensures that all particles will interact with each other when they collide in 2-D and simplifies the calculation of the total interaction energy for colliding particles that we are presenting below.

The actual thickness of the graphene-like particles we model is less than 1 nm,[4] and the aspect ratio of graphene sheets is very high, typically on the order of 10^3.[73] As there is such a large difference in length scales, we ignore the effect of thickness in physical interactions between the particles. Even though the thickness is ignored in physical interactions between different particles, it cannot be ignored for the vdW force calculations as this would mean that the particles are massless and thus exert no force. In the energetic calculations that are presented below, the particles are treated as 1×1 μm^2 plates with a thickness of 1 nm.

The above RCA growth model was used to simulate the experimental results reported in Ref. 24 as summarized in the introduction. The only adjustment we had to do to the model described above to tackle this problem was to calculate the aggregation and deaggregation probability parameters for this particular case. Below, we present the Arrhenius-type relations that were used followed by an explanation of how the aggregation and deaggregation barriers are calculated through the calculation of the energy potential and how we calculate the distance between linear segments by relating it to the coordinates of the particles. The aggregation and deaggregation probabilities are given by Eqs. 1 and 2, respectively

$$P_{agg} = f_1 \, \exp\left(-\frac{E_{agg}}{k_B T} \cdot \frac{1}{f_0}\right) \tag{1}$$

$$P_{deagg} = f_2 \, \exp\left(-\frac{E_{deagg}}{k_B T} \cdot \frac{1}{f_0}\right) \tag{2}$$

where f_0, f_1, and f_2 are constants, and E_{agg} and E_{deagg} are the energy barriers for aggregation and deaggregation, respectively. f_1 and f_2 express the aggregation and deaggregation frequency and f_0 is a scaling factor for the aggregation and deaggregation energy barriers which is used to reduce the total time scale of the aggregation and deaggregation events to make the simulations computationally feasible. More details on the physical and numerical parameters used in our model and the values used for our simulations can be found in Supporting Information Appendix B.

The two energetic barriers are calculated from data of the interaction energy as a function of distance among the colliding particles and then they are simplified to the equivalent step potential barriers as shown in Figure 3. The aggregation energy barrier is equal to the maximum of the interaction energy of a pair of sheets as a function of distance, while the deaggregation barrier is equal to the difference between that maximum and the value of the interaction energy at the distance of 1.5 nm,[24] to account for a steric layer from an adsorbed SDS monolayer (i.e., the distance that is about equal
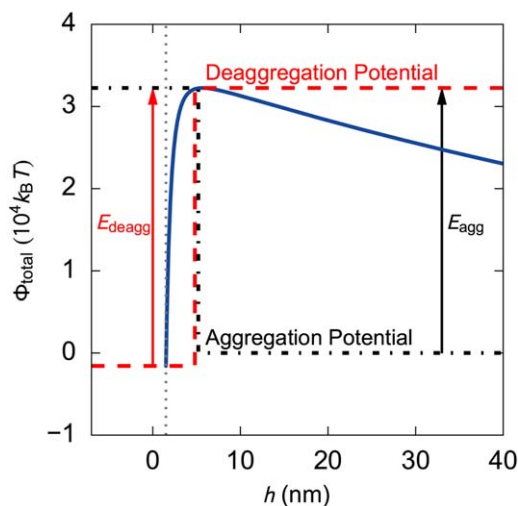

Figure 3. Total energy of interaction of two parallel sheets during collision (blue solid line) and calculation of the respective aggregation (E_{agg}) and deaggregation (E_{deagg}) energies. The dashed red line shows the extracted deaggregation step-potential used by the model while the dashed and dotted black line shows the extracted aggregation step-potential.

Both potentials have the same maximum equal to the maximum of the total energy of interaction. The gray dotted vertical line indicates the assumed steric layer at 1.5 nm. This calculation is repeated for every imminent collision as the relative positions (angle and point of contact) of the particles is different in each case. [Color figure can be viewed at wileyonlinelibrary.com]

to twice the width of a hydrocarbon chain). Assuming that the only effective forces are the vdW attractive forces and the electrostatic repulsive forces, we use the equations calculated for parallel plates of infinite length[74,75] similar to the procedure followed in[24]

$$\varphi_{elec} = 64 k_B T n_b \kappa^{-1} \tanh^2\left(\frac{1}{4}\psi_s\right) \exp(-\kappa h) \tag{3}$$

$$\varphi_{vdW} = -\frac{A}{12\pi}\left[\frac{1}{h^2} + \frac{1}{(h+2d)^2} - \frac{2}{(h+d)^2}\right] \tag{4}$$

$$\Phi_{total} = \int \varphi_{vdW}(h(l))dl + \int \varphi_{elec}(h(l))dl \tag{5}$$

where φ_{elec}, φ_{vdW} are the electrostatic and the vdW potentials per area of the colliding particle, Φ_{total} is the total potential of the colliding particles, n_b is the ion number density, κ^{-1} is the Debye length, ψ_s is the FGS potential which was calculated from the Poisson-Boltzmann equation using measurements of the charge induced on FGS through the adsorption of SDS surfactants,[24] h is the distance between the sheets, A is the Hamaker constant,[76] and d is the thickness of the sheets.

However, in our case, we deviate from the model of parallel plates of infinite length by considering non-parallel sheets as discussed below. Here, h in Eqs. 3 and 4 is now given as h_1 or h_2, depending on whether we calculate distance from the edge or from the main body of the collided particle (as shown in Figure 4), and they are both expressed in terms of the x-coordinate of the particles. This way, we can do the integration along the length of the colliding particle as expressed in Eq. 5
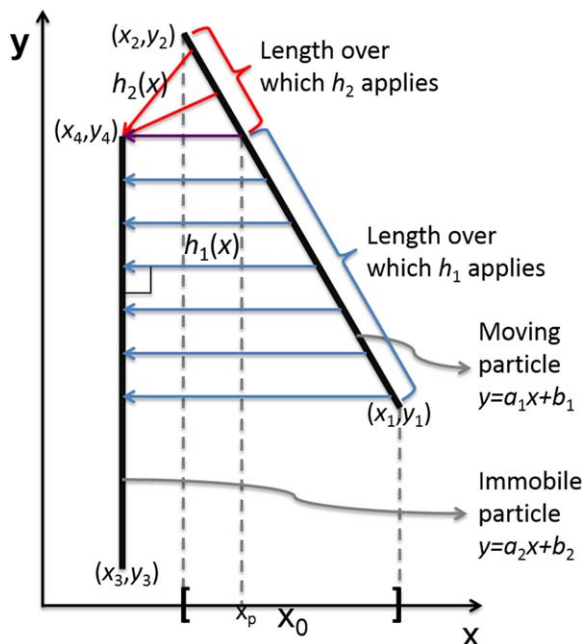
Figure 4. Two line segments are represented with black. The distance as a function of the x-coordinate is represented by the length of the blue arrows for h_1 and by the length of the red arrows for h_2 (in this case, it is the distance from the point (x_4,y_4)).

The purple arrow is taken at the point where $h_1(x_p) = h_2(x_p)$. The h_1 equation is used when $x_p < x < x_1$ while the h_2 equation is used when $x_2 < x < x_p$. In the x-coordinate scale at the bottom the x_0 domain is shown between the brackets (in this case it is $[x_2,x_1]$). [Color figure can be viewed at wileyonlinelibrary.com]

$$h_1 = \frac{|(a_2-a_1)x_0+(b_2-b_1)|}{\sqrt{1+a_1^2}} \quad (6)$$

$$h_2 = \min\left(\sqrt{(a_1x_0+b_1-y_3)^2+(x_0-x_3)^2},\right.$$
$$\left.\sqrt{(a_1x_0+b_1-y_4)^2+(x_0-x_4)^2}\right) \quad (7)$$

for the cases of body-body and edge-body distance calculations, respectively. min(a,b) is a function that outputs a if $a \leq b$ or b if $b < a$. Each line segment is expressed by an equation of the form:

$$y = a_ix+b_i \quad (8)$$

with $i = 1$ for the moving particle (with coordinates of the two edges (x_1,y_1) and (x_2,y_2) and $i = 2$ (with coordinates $[x_3,y_3]$ and $[x_4,y_4]$) for the collided particle. x_0 is the x coordinate of the moving particle ($i = 1$) and varies between x_1 and x_2.

As Eqs. 3 and 4 express the per area interaction energy of a plate that is parallel to an infinite plate, we decreased the values of these equations by a factor of 10^2 (which is factored in f_0 - for details see Supporting Information Appendix B) to approximate the per area interaction energy of an infinitesimal plate interacting with a finite plate and then we integrate the infinitesimal plate interaction along the length of the colliding particle (x_0) to take the angle difference into account. This procedure is equivalent to considering each particle as a sum of infinitesimal parts that are all parallel to their interacting particle.

When a collision of two sheets (either single sheets or sheets that are part of a cluster) is imminent, the above energetic calculation is performed in order to calculate the interaction energy for different distances between the sheets. From these data, we calculate the aggregation and deaggregation energies between the two particles as shown in Figure 3. These values are substituted into Eqs. 1 and 2 to calculate the probability for aggregation and deaggregation, respectively. The aggregation probability value defines whether these particles/clusters will collide, in which case they aggregate and merge in one cluster, or they will not collide at all. The deaggregation probability value, in case of a successful collision, defines the probability that the aggregated particles may deaggregate in future steps.

For computational simplicity, we assume that deaggregation of a particle signals deaggregation from all its neighbors simultaneously, following the SAK model.[49] The overall deaggregation barrier (E_{deagg}) is assumed to be equal to the sum of the deaggregation barriers that were calculated during the collision of each pair of particles that is part of the deaggregation process. In order for deaggregation to occur in this way, it was necessary to assume that the deaggregation barrier calculation is independent to the direction of the deaggregating step. This is not very far from the truth as the maximum of the energy barrier is always very close to the point of collision, which means that the relative positions between the deaggregating sheets are close to the relative positions of the aggregating sheets. Thus, the parameters that matter the most in the calculation of the aggregation and the deaggregation barriers are the point of collision and the angle created by the two particles at that point and not the angle of the relative movement between them.

The transformation of the continuous potential to a step potential barrier for aggregation and a step potential barrier for deaggregation, as seen in Figure 3, reduces the computational load and even though we expect it to affect the dispersion of the particles around clusters we do not expect it to affect their size and structure. The main effect of this assumption is that during the collision of clusters the only energetic calculation that is performed is between the collided particles.

In summary, the assumptions of this model and the assumptions introduced to tackle this particular problem are:

1. The system is simplified to 2-D and the graphene particles, that are normally nonflat sheets, are represented by straight and rigid line segments. These represent plate-like particles that are concentric and parallel with respect to the dimension perpendicular to the plane and their thickness is ignored during physical interactions.

2. The only acting forces are vdW and electrostatic.

3. The equations of interaction forces for plates of infinite length are assumed to be valid for particles of finite length and for edge-body interactions after a reduction by a factor.

4. Forces are only effective during collision and deaggregation attempts. During a collision, the only energetic calculation is between the two colliding particles, which have to overcome the aggregation barrier to form a new cluster.

5. There is a steric barrier of 1.5 nm between the particles due to adsorbed SDS.

6. During deaggregation, we assume that the energy for deaggregation is the sum of the calculated deaggregation energies between the particle that tries to deaggregate and all its direct neighbors (the particles it was in direct contact with at that point). For each case, the deaggregation energy
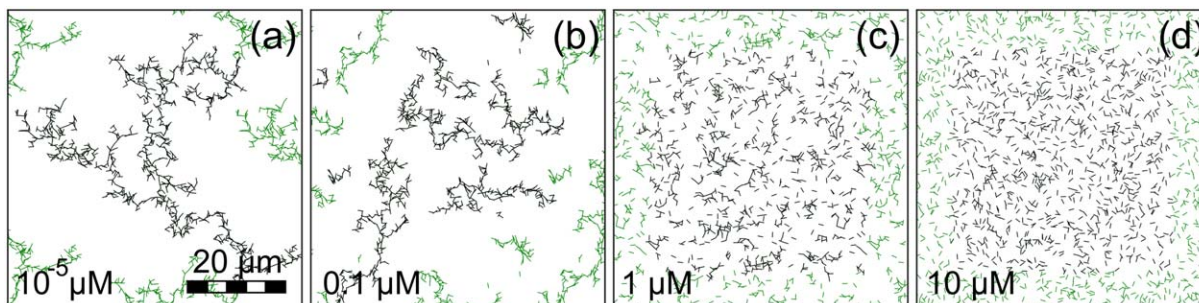
Figure 5. Images from simulations for different surfactant concentrations with constant concentration of particles (~0.49 particles/μm^2, 1,000 particles in a 45 x 45 μm matrix at the step 6 × 10^6).

Particles that are parts of the neighboring simulation domains (the boundary conditions are periodic) appear in green. Particles that belong to clusters that have crossed the boundaries and reappear on the other side appear also in green and their unconnected parts have been moved back to show the complete shape of each cluster and appear in black. All other particles that are part of the main simulation domain appear in black. [Color figure can be viewed at wileyonlinelibrary.com]

is assumed to be independent of the angle of the relative movement between the deaggregating particles.

7. The diffusion coefficient does not depend on the direction that the particles move and there are no effects from the liquid medium.

8. Sedimentation only happens during centrifugation and thus gravitational forces are ignored in our simulation, although gravitational effects are considered later in the Results and Discussion section once the resulting structures are determined.

Results and Discussion

We first present the results of our simulations from the implementation of the above RCA model by comparing the cluster structures to the optical microscopy images of Figure 1 and presenting how the cluster size changes with surfactant concentration and time. Then, we show the change in gravimetric Peclet number, Pe_g, of the clusters with surfactant concentration and time and explain why at C_{crit} a high percentage of the particles is expected to sediment early as shown in Figure 2 and for lower surfactant concentration we show a densification of the clusters with time that can lead to sedimentation of the formed gel later in time. Finally, we discuss the behavior of our model in terms of aggregation and deaggregation rates and explain that even though we have not reached equilibrium we do not expect the clusters formed at high C to grow further due to their dynamic nature.

Cluster size and critical concentration

In Figure 1, we presented the different structures that are observed under optical microscope for different surfactant concentrations right after sonication of the samples. These structures varied from highly ramified aggregates at low surfactant concentrations, to dense aggregates around C_{crit}, and to well-dispersed suspensions for even higher surfactant concentrations. Figure 5 shows equivalent structures of clusters produced by our model. The different surfactant concentrations correspond to different inter-particle forces and all results are captured at the 6 × 10^6 simulation step which corresponds to about half minute of experimental time (see Supporting Information Appendix C for calculation of diffusion time scale). In this case, two main types of structures are identified: ramified clusters (Figures 5a, 5b) of average size that decreases with surfactant concentration and dispersed single or few-layer particles (Figure 5d).

To determine the growth rate of the clusters for different surfactant concentrations, we determine the average number of particles per cluster ($\bar{s}$) as a function of time as shown in Figure 6. At short times, the lower the surfactant concentration, the higher the net aggregation rate (i.e., the rate of change in average cluster size) is. For surfactant concentrations of 10^{-5} and 0.1 μM, the average cluster size follows a similar pattern, with the low concentration having clearly higher net aggregation rate initially. At longer times, however, both systems reach the same limit as growth eventually stops near the limit of total number of particles in the system (with the
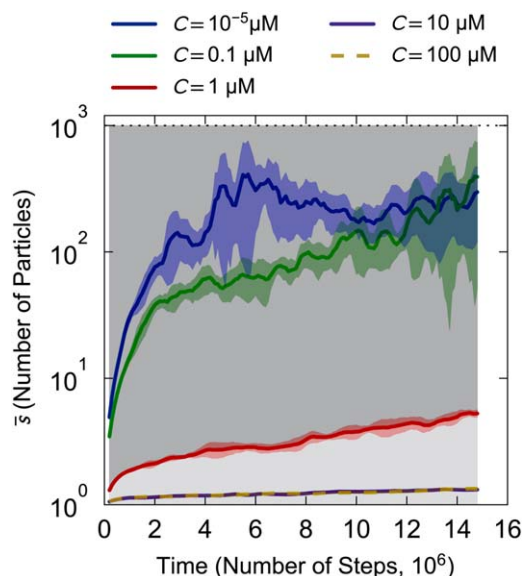

Figure 6. Results from simulations for different surfactant concentrations with constant concentration of particles (~0.49 particles/μm^2, 1000 particles in a 45 x 45 μm matrix).

The vertical axis depicts the average number of particles per cluster while the horizontal axis represents the simulation time. The dotted black horizontal line indicates the maximum cluster size, equal to the total number of particles (1000). These data represent the 5-point moving average of the average values from 3 simulations with the standard deviation of the 3 values drawn as a faded region around each corresponding line. The dark gray region indicates the aggregated state and the light gray region marks the dispersed state. [Color figure can be viewed at wileyonlinelibrary.com]

system $C = 10^{-5}$ μM reaching that limit earlier due to higher aggregation rate). Growth rate generally slows with time in each case, independent of concentration. This reduction in growth rate was expected due to a decrease in the number of single particles in the system. The clusters that are formed have higher intercluster distances and diffuse slower relative to the single particles that existed initially.

Above a surfactant concentration of 0.1 μM, there is a sudden drop in the cluster growth rates with surfactant concentration. At the 10 and 100 μM concentrations, cluster growth is nearly zero for high simulation times, corresponding to the dispersed states observed in Figure 5c. Once a thermodynamically stable dispersed state is achieved, we expect the clusters to stop growing and remain embryonic.[77] The results in Figure 6 suggest that we have not yet reached this equilibrium state in our simulations and discuss this claim further in the last subsection of Results and Discussion by looking at the average cluster lifetime.

The transition from fast growth (at short times) to slow or no cluster growth regime helps us to identify a region of sudden change in the net aggregation rate pattern between the SDS concentrations of 0.1 and 10 μM. A transition from fast cluster growth regime to almost zero growth takes place in this region. At this intermediate concentration ($C = 1$ μM), there also appears to be a significant number of small clusters of size 10 μm and smaller just like in case (iii) (Figure 1c). Thus, we have two indications (a transition zone in growth rate and 10 μm-sized clusters) that $C = 1$ μM is the critical concentration as predicted from our model. One more characteristic of the critical concentration is that it tends to produce denser aggregates (as seen in Figure 1) that lead to more particles sedimenting and thus lower UV-Vis absorbance (as seen in Figure 2). We quantify this claim in the following subsection by calculating the Pe_g of clusters and noting its shift with SDS concentration.

Cluster sedimentation

Traditionally, Pe_g has been used as the sedimentation metric in colloidal science.[74] Pe_g expresses the balance between Brownian motion and buoyancy versus gravity. A Pe_g value of 1 or lower is indicative of non-sedimenting individual particles while a value a lot higher than 1 indicates strong gravitational forces and therefore fast sedimentation. We define the Pe_g of an individual particle as defined in[74]

$$Pe_g = \frac{4\pi\Delta\rho\alpha^3 g l_c}{3k_B T} \tag{9}$$

where $\Delta\rho$ is the difference in density between the particle and the solution, α is the hydrodynamic radius of the particle, g is the gravitational acceleration and l_c is a characteristic sedimentation distance, which we take to be equal to 1 mm, which is an order of magnitude higher than the length of our simulation domain.

To evaluate whether the clusters generated by our model sediment or not we generalized Eq. 9 to calculate Pe_g for clusters. For this, we substituted α with radius of gyration, R_g of the cluster instead of its hydrodynamic radius since these numbers are close to each other and the former is easier to calculate. The density of the clusters was calculated as the ratio of total mass of graphene particles and water occupying the volume not-occupied by the particles over the total volume. The volume of the clusters is assumed to be equal to the volume of a disk with a radius of R_g and thickness equal to the length of

one graphene particle (l). This is consistent with our existing assumption of treating our individual particles as 1×1 μm² plates with a fixed 1 μm depth in the direction perpendicular to the 2D plane

$$R_g^2 = \frac{1}{N}\sum_{i=1}^{N} R_i^2 \tag{10}$$

$$\rho = \frac{N m_{fgs} + \left(\pi R_g^2 l - N V_{fgs}\right)\rho_w}{\pi R_g^2 l} \tag{11}$$

where N is the total number of particles of the cluster, R_i is the distance between the center of each particle and the center of mass of the cluster, m_{fgs}, the mass of one FGS, l is the length of the graphene sheets in the dimension perpendicular to the 2D plane (i.e., 1 μm), V_{fgs} is the volume of one FGS, and ρ_w is the density of water. m_{fgs} was taken equal to 8.178×10^{-16} g for a 1 μm² FGS area, assuming an area of a carbon hexagon of 5.239×10^{-8} μm² and a C/O ratio of 18. V_{fgs} is 7×10^{-4} μm³ assuming an area of 1 μm² and a thickness of 0.7 nm. Even though it is hard to calculate the exact thickness of FGS, XRD data show that the interlayer spacing of graphite oxide increases to 0.7 nm during the oxidation of graphite.[73] The average values for R_g and ρ calculated for our clusters are included in Supporting Information Appendix D (Figures S2 and S3).

We note that our goal is not to model the simultaneous aggregation and sedimentation processes. There are modeling and experimental efforts that have focused on this challenging problem.[78,79] Our approach is to ignore sedimentation first during the aggregation process and to simply evaluate a sedimentation metric that would tell us how prone to sedimentation clusters and particles are.

The cluster-Pe_g metric helped us correlate our simulation data to the UV-Vis absorbance data of Figure 2 where we see that the supernatant becomes highly transparent around C_{crit}. Below that concentration, the supernatant becomes transparent at a slower rate and above C_{crit} the absorbance does not decrease significantly throughout a year. Experimentally, persisting high UV-Vis absorbance values of the supernatant indicate very slow sedimentation or no sedimentation with time. This can happen (1) when a contiguous connected particle network, for example, a gel structure or (2) dispersed particles or dispersed ramified particle clusters with a low enough Peclet number form. In the first case, while strong gels can resist sedimentation, they can densify with time, shrink, and sediment. In the second case, dispersed ramified clusters may also restructure with time, densify, and sediment at a faster rate as their Peclet number increases and single particles may form dense clusters later on. Thus, while high UV-Vis absorbance corresponds to systems that resist sedimentation either due to the formation of a contiguous network structure or dispersed low Pe_g particles/clusters, low UV-Vis absorbance values relate to dense aggregate systems.

A metric that is useful for a comparison of our results with the absorbance data of Figure 2 is the percentage of particles that belong to clusters with a Pe_g number higher than 1. Those are the clusters that would tend to sediment because of the relative high gravimetric forces that they experience. In Figure 7, we present how this metric varies with simulation time and surfactant concentration. The higher the percentage of particles that belong to high Pe_g clusters, the higher the percentage of particles that might sediment, as long as a strong gel that resists sedimentation is not formed.
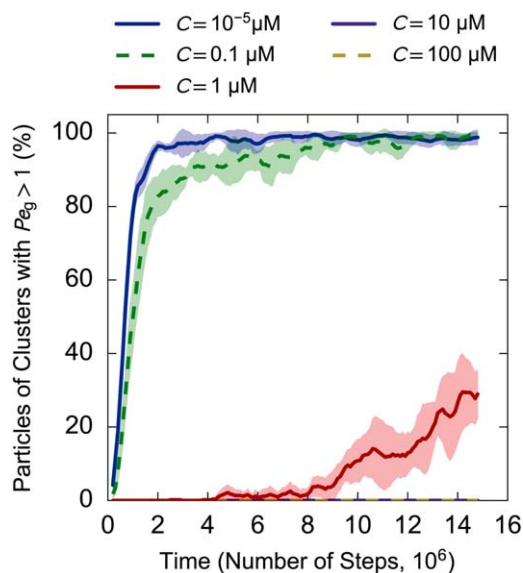
Figure 7. Results from simulations for different surfactant concentrations with constant concentration of particles (~0.49 particles/μm^2, 1000 particles in a 45 × 45 μm matrix).

These data represent the 5-point moving average of the average values from 3 simulations with the standard deviation of the 3 values drawn as a faded region around each corresponding line. The vertical axis presents the percentage of sheets that belong to clusters with Pe_g that exceeds the value of 1 (i.e., gravimetric force is more important than Brownian motion) as a function of time. [Color figure can be viewed at wileyonlinelibrary.com]

As we see in Figure 7, the percentage of particles associated with clusters of high Pe_g decreases with increasing SDS concentration. At $C = 10$ and 100 μM, $Pe_g \ll 1$ and thus sedimentation is not expected in agreement with experimental data in Figure 2. Similarly, Figure 6 shows that at 10^{-5} and 0.1 μM particles tend to organize in large clusters. This is an indication for the formation of a gel network, given a large enough particle concentration, which also prevents sedimentation of those particles.

However, at the SDS concentration of 1 μM, there is a significant percentage of particles with $Pe_g > 1$ that can sediment as they do not form large clusters as in lower surfactant concentrations. The average size of clusters formed for the time scale of our simulations remains below 10 particles per cluster. This means that, for SDS concentrations around 1 μM a gel is not formed for the time scale of our simulation and the number of clusters with high Pe_g that are formed will be free to sediment. This observation also agrees with the data from Figure 2 that show a decrease in UV-Vis absorbance around the critical surfactant concentration.

For $C = 1$ μM, we also see that the rate of formation of clusters that can sediment is much lower than for lower surfactant concentrations but it is non-zero. The entire length of our simulation (15 million steps) corresponds to about 1.5 min (according to the approximate calculation shown in Supporting Information Appendix C) and an average of 30% of particles belongs to clusters that can sediment. Comparing that with Figure 2 the green line shows that a significant percentage of particles will sediment in 1 h at C_{crit} (about 10 μM for experimental case). Our simulation might have overestimated the rate of creation of dense clusters at C_{crit} (about 1 μM for

our simulation), since 1 h of real time corresponds to 631 million simulation steps; But, we cannot be entirely sure since no results were collected for smaller times (except right after dispersion).

A more appropriate metric for gelation would be the gravimetric Peclet number as defined by Poon and Haw[80], if the right critical value were known for our system. A critical gravimetric Peclet value below which gelation occurs was calculated by Kim et al.[81] for the case of adhesive spheres but not for our case of linear particles that experience attractive and repulsive forces.

Combining the cluster size information of Figure 6 and a sedimentation analysis of the percentage of particles based on Pe_g, we have addressed the low absorbance values for C_{crit} in Figure 2 at a given time; but, we have not yet addressed the drop in absorbance with time for $C < C_{crit}$. In order to address this slow sedimentation behavior that occurs at lower surfactant concentrations, we will now consider a local densification through restructuring in the next subsection.

Densification through restructuring

To investigate the local density of the particle clusters with time, we introduce a new metric: the average angle formed between neighboring particles. This presents the mean of the angle formed between each pair of directly neighboring particles within each cluster (i.e., particles that are in contact with each other). An angle difference of 90° indicates vertically oriented neighboring particles, while an angle difference of 0 indicates parallel neighboring particles. Clusters with lower average angle difference consist of particles that are on average closer to each other tending towards a layered and thus denser structure. This gives us a better idea of the local density of the clusters as it indicates how close neighboring particles are to each other.

Figure 8 shows how the average angle varies with time for different surfactant concentrations. First important observation is that the average angle of the neighboring particles increases with surfactant concentration. This is a result of the nonlinear relation between E_{agg} and P_{agg} as expressed in Eq. 1. Generally, E_{agg} increases with increasing surfactant concentration because of the ψ_s term that appears in Eq. 3. This translates to different P_{agg} distributions as a function of average angle of neighboring particles for each surfactant concentration. The result is a lower probability for neighboring particles to form small angles as the surfactant concentration (and therefore the intensity of repulsive forces) increases. This behavior is observed even for really low times as we start with a well-dispersed system and there are no pre-existing clusters that would affect our results.

Another observation from Figure 8 is that for surfactant concentrations below 1 μM, there is a clear continuous drop of average angle difference with time indicating densification through restacking, while there is no clear indication of reduction of this metric with time for surfactant concentrations above 1 μM. We attribute this drop to a sampling of more states between clustered particles. When a particle deaggregates from the interior of a large cluster there is a larger chance that this particle will collide again with the same cluster and reaggregate with it in a different angle. Overall, smaller angles have higher Φ_{total} due to larger area interactions and, as we see from Figure 3, this leads to higher E_{agg} and to lower deaggregation probabilities (as seen from Eq. 2), and, therefore, bonds of smaller angles tend to survive longer.

This densification behavior can be correlated to the real system. As in Figure 2, there is a clear reduction in absorbance
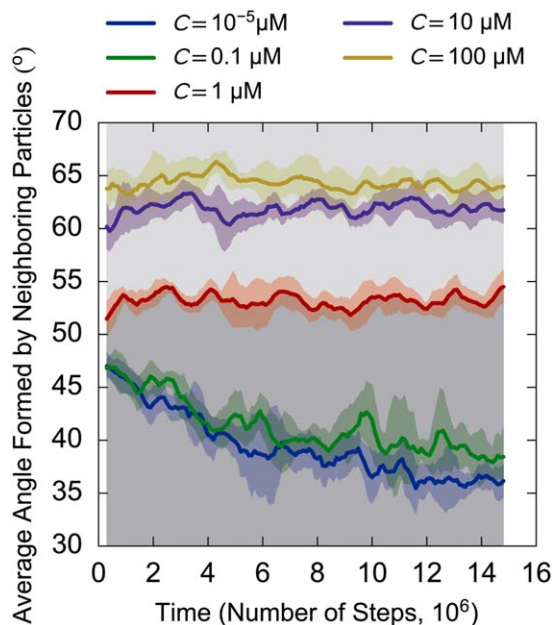
Figure 8. Results from simulations for different surfactant concentrations with constant concentration of particles (~0.49 particles/μm², 1000 particles in a 45 × 45 μm matrix).

The vertical axis presents the average angle difference between neighboring aggregated particles as a function of time. The dark gray region indicates the aggregated state and the light gray region marks the dispersed state. [Color figure can be viewed at wileyonlinelibrary.com]

and thus sedimentation with time for samples of surfactant concentration lower than the critical surfactant concentration. Combining the results from the current and the previous subsection, we can better explain the experimental results of Figure 2: At the critical concentration, a large number of high Pe_g clusters is formed and those clusters sediment. Below that SDS concentration, a gel is formed given a high enough concentration of particles. With time, these gels densify and tend to form more graphite-like structures that will eventually sediment. According to Figure 2, sedimentation of particles for low surfactant concentrations happens with a slower rate. The reason for the difference in sedimentation rates can be attributed to the time scale difference of the two mechanisms that produce those sedimenting clusters.

Aggregation and deaggregation rates

The aggregation and deaggregation probabilities as defined in Eqs. 1 and 2 are basically the probabilities of an aggregation or deaggregation event occurring given that a collision or a deaggregation attempt has occurred, respectively. In order to calculate the net aggregation rate ($r_{n,agg}$) we first calculated the aggregation rate (r_{agg}) by multiplying the aggregation probability with the rate of collisions and the deaggregation rate (r_{deagg}) by multiplying the deaggregation probability with the rate of deaggregation attempts. $r_{n,agg}$ is the difference between r_{agg} and r_{deagg}

$$r_{n,agg} = r_{agg} - r_{deagg} =$$
$$= P_{agg} r_{collision} - P_{deagg} r_{deagg,att} \quad (12)$$

where P_{agg} and P_{deagg} are the average values of the probabilities defined in Eqs. 1 and 2. $r_{collision}$ is the rate of imminent

collisions (this includes potential collisions that did not happen because the aggregation barrier was not crossed), and $r_{deagg,att}$ the rate of deaggregation attempts, that is, the rate at which a particle will be tested for deaggregation with its neighbors (equivalent to rate of collisions for aggregation). As we mentioned in the Model and Application section, in each step, we pick a particle at random for deaggregation and if this particle is part of a cluster we attempt to deaggregate it from its neighbors. Therefore, the rate of deaggregation attempts, $r_{deagg,att}$ is equal to the percentage of particles that belong to clusters (i.e., particles that are not single).

In Figure 9, we present how the average aggregation and deaggregation rates change with time and surfactant concentration. Figure 9a shows the values of r_{agg}. As expected from Figure 6, the higher the value of surfactant concentration the lower the value of r_{agg}. For low surfactant concentrations, we observe a decrease of r_{agg} with time, while for high surfactant concentrations, it remains almost constant. The decrease for low C can be attributed to the fact that fewer free particles remain in the matrix with higher relative distances from each other, which causes a decrease in collision rate. This makes aggregation events more rare with time. This phenomenon is not observed for high C as the size of the clusters does not change significantly with time. The initial jump we see in r_{agg} for all surfactant concentrations can be attributed to an averaging starting with values of zero at zero-time step. In the cases of $C = 10^{-5}$ and 0.1 μM, the initial increase is accompanied by a fast decrease for times below the millionth-time step. This is again due to the increase in cluster size which happens at a high rate at these concentrations and times.

Figure 9b shows r_{deagg}, which follows a similar trend to r_{agg}. For low C, we see a decrease of r_{deagg} with time, while for high C, r_{deagg} remains relatively constant with time. This decrease in the rate of deaggregation events can be attributed to a decrease in the deaggregation probability. The larger the clusters the larger the percentage of particles that are in the interior of those clusters. Particles that are in the interior of the clusters have a larger number of neighbors and thus a lower probability to deaggregate. The initial increase in r_{deagg} that is observed for all surfactant concentrations is real (as opposed to the one observed in Figure 9a) and is caused by the
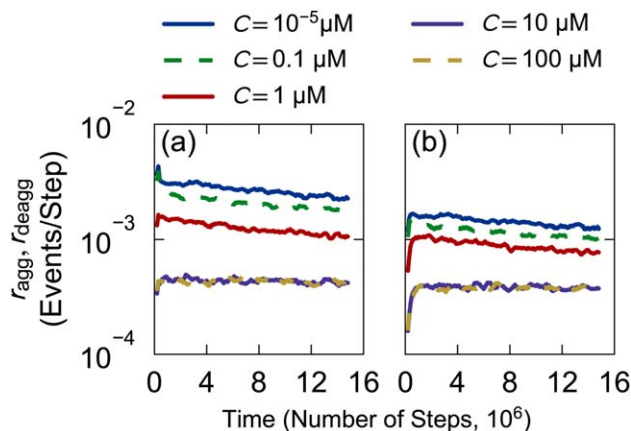

Figure 9. (a) Rate of aggregation calculated using the variables shown in Eq. (12).

(b): Rate of deaggregation as calculated by the variables in Eq. 12. These data represent the 5-point moving average of the average values from 3 simulations. [Color figure can be viewed at wileyonlinelibrary.com]

fact that we start with a dispersed system and the existence of clusters is a prerequisite for deaggregation to occur.

An aggregation event is not necessarily equivalent to a deaggregation event. An aggregation event is the result of the collision of two particles (that might be single particles or part of a cluster) that merge into one cluster. A deaggregation event is a result of a succesful deaggregation attempt between a particle that belongs to a cluster and all its direct neighbors. This means that a deaggregation event results in the separation of a cluster in two or more clusters, while an aggregation event always merges two clusters/particles into one. Therefore, we expect r_{agg} to maintain higher values than r_{deagg} even during equilibrium.

Further, even though r_{deagg} has higher values for lower C, this does not mean that the large clusters formed at these surfactant concentrations are more dynamic than the ones for high C. One metric that can help us quantify the dynamic nature of the clusters formed in our model is the average cluster lifetime (τ_c)

$$\tau_c = \frac{\bar{s}}{r_{deagg}} \qquad (13)$$

where $\bar{s}$ is the average cluster size. This value approximates the time for an average cluster (in each surfactant concentration and time) to deaggregate completely.

Figure 10 shows how the average cluster lifetime changes with time and surfactant concentration. For low C, the lifetime of the clusters is high and is getting larger as their size grows. For high surfactant concentration, their size remains low with time. This indicates that the small clusters formed at these surfactant concentrations are very dynamic comparing to the large clusters formed at lower C. The initial drop in the value of lifetime is caused by the initial increase in deaggregation rates observed in Figure 9.
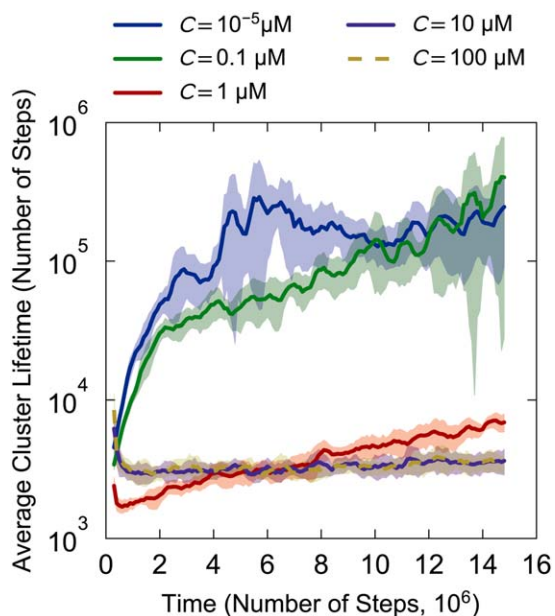

Figure 10. Change of the average cluster lifetime as calculated by Eq. 13.

These data represent the 5-point moving average of the average values from 3 simulations with the standard deviation of the 3 values drawn as a faded region around each corresponding line. [Color figure can be viewed at wileyonlinelibrary.com]

At $C = 1$ μM, Figure 10 reveals an interesting behavior: At initial times, as the clusters remain small they are more dynamic than the clusters formed at high C. As the cluster size grows their lifetime exceeds the lifetime of clusters formed at higher C. The fact that clusters appear more dynamic at $C = 1$ μM than at higher C is not necessarily representative of the physical reality but is indicative of how our model works, that is, allowing restructuring of the clusters through continuous deaggregations and reaggregations. In real systems, a lot of this restructuring happens by bending[82] of graphene particles and their relative movement to each other without deaggregation really occurring.

Overall, none of our simulations has reached equilibrium. For low surfactant concentrations r_{agg} and r_{deagg} are decreasing continuously (Figure 9) and the relative angles of neighboring particles are also decreasing (Figure 8). For lower surfactant concentrations, the size of the clusters is increasing (Figure 6), although slowly. Nevertheless, from Figure 10 we conclude that the small clusters that are created at high surfactant concentrations have a very short life time, are very dynamic, and they do not grow further as they never go beyond an embryonic cluster stage. Embryo clusters are expected to form even in thermodynamically stable dispersed colloidal suspensions due to random fluctuations in our system that can be explained by statistical mechanics.[77]

Finally, we expect the initial concentration of particles to have an effect on the aggregation and the deaggregation rates. More specifically, a lower initial particle concentration would lead to lower aggregation rates due to the larger initial distances between the particles. This lower aggregation rate also leads to lower deaggregation rates because the rate of deaggregation attempts is proportional to the number of aggregated particles, as mentioned earlier. Overall, we do not expect the initial particle concentration to have an effect on the behavior of the system, other than reducing the overall size of the clusters (due to the reduced number of available particles) and reducing both the aggregation and deaggregation rates.

Conclusions

This is the first reversible aggregation model for non-linear particles and it can help in building intuition on problems about graphene-like or other atomically thin particle aggregation or needle(rod)-like particles aggregation that move on the same 2-D plane (e.g., an interface).

Both the experiments and the simulations give us similar trends related to the particle cluster size, an indication for the existence of a critical concentration of surfactant at which many dense clusters are formed, an indication for the formation of a gel below that concentration which tends towards a graphite-like structure with time and mostly dispersed single particles above the critical surfactant concentration.

One point of disagreement between experiments and simulations is the actual value of the critical surfactant concentration: the experiments indicate that this value is about 10 μM of SDS while the simulations point towards a value in the order of 1 μM. A quantitative disagreement is something that was expected based on the number and weight of our assumptions and especially since our simulations are performed in 2D. At $C > C_{crit}$, our model captures the state of a thermodynamically stable colloidal dispersion well with the formation of embryonic clusters with very short life times that never reach the stable cluster (nucleus) size.

The assumption that probably had the largest effect on our results is the rigid nature of graphene. In reality, we know that graphene particles that come in touch with each other find a favorable position really fast as the particles are able to fold and bend to get to more energetically favorable positions. What we do instead is to sample different energetic states by allowing deaggregation and reaggregation of the particles. This is something that we expect to have a significant effect on the time scales of the results generated by our RCA model.

Our approach ignored the effect of flow since it was not relevant to the modeled experiments; but, flow effects can be incorporated in our algorithm by altering the diffusion step size and probability of moving in different directions for each step.

Acknowledgments

Literature Cited

1. Novoselov KS, Geim AK, Morozov SV, Jiang D, Zhang Y, Dubonos SV, Grigorieva IV, Firsov AA. Electric field effect in atomically thin carbon films. *Science*. 2004;306(5696):666–669.
2. Hwa T, Kokufuta E, Tanaka T. Conformation of graphite oxide membranes in solution. *Phys Rev A*. 1991;44(4):R2235–R2238.
3. Zhang C, Dabbs DM, Liu L-M, Aksay IA, Car R, Selloni A. Combined effects of functional groups, lattice defects, and edges in the infrared spectra of graphene oxide. *J Phys Chem C*. 2015;119(32): 18167–18176.
4. Schniepp HC, Li J-L, McAllister MJ, Sai H, Herrera-Alonso M, Adamson DH, Prud'homme RK, Car R, Saville DA, Aksay IA. Functionalized single graphene sheets derived from splitting graphite oxide. *J Phys Chem B*. 2006;110(17):8535–8539.
5. Sabourin JL, Dabbs DM, Yetter RA, Dryer FL, Aksay IA. Functionalized graphene sheet colloids for enhanced fuel/propellant combustion. *ACS Nano*. 2009;3(12):3945–3954.
6. Stankovich S, Dikin DA, Dommett GHB, Kohlhaas KM, Zimney EJ, Stach EA, Piner RD, Nguyen ST, Ruoff RS. Graphene-based composite materials. *Nature*. 2006;442(7100):282–286.
7. Ramanathan T, Abdala AA, Stankovich S, Dikin DA, Herrera-Alonso M, Piner RD, Adamson DH, Schniepp HC, Chen X, Ruoff RS, Nguyen ST, Aksay IA, Prud'Homme RK, Brinson LC. Functionalized graphene sheets for polymer nanocomposites. *Nat Nanotechnol*. 2008;3(6):327–331.
8. Kim H, Abdala AA, Macosko CW. Graphene/Polymer Nanocomposites. *Macromolecules*. 2010;43(16):6515–6530.
9. Wang D, Choi D, Li J, Yang Z, Nie Z, Kou R, Hu D, Wang C, Saraf LV, Zhang J, Aksay IA, Liu J. Self-assembled TiO₂-graphene hybrid nanostructures for enhanced Li-ion insertion. *ACS Nano*. 2009;3(4):907–914.
10. Wang H, Cui L-F, Yang Y, Sanchez Casalongue h, Robinson JT, Liang Y, Cui Y, Dai H. Mn₃O₄-graphene hybrid as a high-capacity anode material for lithium ion batteries. *J Am Chem Soc*. 2010; 132(40):13978–13980.
11. Wu Z-S, Ren W, Wen L, Gao L, Zhao J, Chen Z, Zhou G, Li F, Cheng H-M. Graphene anchored with Co₃O₄ nanoparticles as anode of lithium ion batteries with enhanced reversible capacity and cyclic performance. *ACS Nano*. 2010;4(6):3187–3194.
12. Park M-S, Yu J-S, Kim KJ, Jeong G, Kim J-H, Jo Y-N, Hwang U, Kang S, Woo T, Kim Y-J. One-step synthesis of a sulfur-impregnated graphene cathode for lithium-sulfur batteries. *Phys Chem Chem Phys*. 2012;14(19):6796–6804.
13. Pope MA, Aksay IA. Structural design of cathodes for Li-S batteries. *Adv Energy Mater*. 2015;5(16):1500124
14. Zhu Y, Murali S, Stoller MD, Ganesh KJ, Cai W, Ferreira PJ, Pirkle A, Wallace RM, Cychosz KA, Thommes M, Su D, Stach EA, Ruoff RS. Carbon-based supercapacitors produced by activation of graphene. *Science*. 2011;332(6037):1537–1541.
15. Pope MA, Korkut S, Punckt C, Aksay IA. Supercapacitor electrodes produced through evaporative consolidation of graphene oxide-water-ionic liquid gels. *J Electrochem Soc*. 2013;160(10):A1653–A1660.
16. Wang Y, Shi Z, Huang Y, Ma Y, Wang C, Chen M, Chen Y. Supercapacitor devices based on graphene materials. *J Phys Chem C*. 2009;113(30):13103–13107.
17. Wang X, Zhi L, Müllen K. Transparent, conductive graphene electrodes for dye-sensitized solar cells. *Nano Lett*. 2008;8(1):323–327.
18. Wu J, Becerril HA, Bao Z, Liu Z, Chen Y, Peumans P. Organic solar cells with solution-processed graphene transparent electrodes. *Appl Phys Lett*. 2008;92(26):263302
19. Tölle FJ, Fabritius M, Mülhaupt R. Emulsifier-free graphene dispersions with high graphene content for printed electronics and free-standing graphene films. *Adv Funct Mater*. 2012;22(6):1136–1144.
20. Torrisi F, Hasan T, Wu W, Sun Z, Lombardo A, Kulmala TS, Hsieh G-W, Jung S, Bonaccorso F, Paul PJ, Chu D, Ferrari AC. Inkjet-printed graphene electronics. *ACS Nano*. 2012;6(4):2992–3006.
21. Dua V, Surwade SP, Ammu S, Agnihotra SR, Jain S, Roberts KE, Park S, Ruoff RS, Manohar SK. All-organic vapor sensor using inkjet-printed reduced graphene oxide. *Angew Chem Int Ed Engl*. 2010;49(12):2154–2157.
22. Hernandez Y, Nicolosi V, Lotya M, Blighe FM, Sun Z, De S, McGovern IT, Holland B, Byrne M, Gun'Ko YK, Boland JJ, Niraj P, Duesberg G, Krishnamurthy S, Goodhue R, Hutchison J, Scardaci V, Ferrari AC, Coleman JN. High-yield production of graphene by liquid-phase exfoliation of graphite. *Nat Nanotechnol*. 2008;3(9): 563–568.
23. Parviz D, Das S, Ahmed HST, Irin F, Bhattacharia S, Green MJ. Dispersions of non-covalently functionalized graphene with minimal stabilizer. *ACS Nano*. 2012;6(10):8857–8867.
24. Hsieh AG, Korkut S, Punckt C, Aksay IA. Dispersion stability of functionalized graphene in aqueous sodium dodecyl sulfate solutions. *Langmuir*. 2013;29(48):14831–14838.
25. Hsieh AG, Punckt C, Aksay IA. High-rate Li+ storage capacity of surfactant-templated graphene-TiO₂ nanocomposites. *J Electrochem Soc*. 2015;162(8):A1566–A1573.
26. Stankovich S, Piner RD, Chen X, Wu N, Nguyen ST, Ruoff RS. Stable aqueous dispersions of graphitic nanoplatelets via the reduction of exfoliated graphite oxide in the presence of poly(sodium 4-styrenesulfonate). *J Mater Chem*. 2006;16(2):155–158.
27. Kim H, Miura Y, Macosko CW. Graphene/polyurethane nanocomposites for improved gas barrier and electrical conductivity. *Chem Mater*. 2010;22(11):3441–3450.
28. Sayyar S, Murray E, Thompson BC, Gambhir S, Officer DL, Wallace GG. Covalently linked biocompatible graphene/polycaprolactone composites for tissue engineering. *Carbon N Y*. 2013;52: 296–304.
29. Tang L-C, Wan Y-J, Yan D, Pei Y-B, Zhao L, Li Y-B, Wu L-B, Jiang J-X, Lai G-Q. The effect of graphene dispersion on the mechanical properties of graphene/epoxy composites. *Carbon N Y*. 2013;60:16–27.
30. Fornes TD, Paul DR. Modeling properties of nylon 6/clay nanocomposites using composite theories. *Polymer (Guildf)*. 2003;44(17): 4993–5013.
31. Derksen JJ. Direct numerical simulations of aggregation of mono-sized spherical particles in homogeneous isotropic turbulence. *AIChE J*. 2012;58(8):2589–2600.
32. Natale G, Heuzey MC, Carreau PJ, Ausias G, Férec J. Rheological modeling of carbon nanotube suspensions with rod-rod interactions. *AIChE J*. 2014;60(4):1476–1487.
33. Cwalina CD, Harrison KJ, Wagner NJ. Rheology of cubic particles in a concentrated colloidal dispersion suspending medium. *AIChE J*. 2017;63(3):1091–1101.
34. Rudd RE, Broughton JQ. Coarse-grained molecular dynamics and the atomic limit of finite elements. *Phys Rev B*. 1998;58(10):R5893–R5896.
35. Kaunisto E, Rasmuson A, Bergenholtz J, Remmelgas J, Lindfors L, Folestad S. A simple model for simulation of particle deaggregation of few-particle aggregates. *AIChE J*. 2014;60(5):1863–1869.
36. Hoogerbrugge PJ, Koelman JMVA. Simulating microscopic hydrodynamic phenomena with dissipative particle dynamics. *Europhys Lett*. 1992;19(3):155–160.
37. Brady JF, Bossis G. Stokesian dynamics. *Annu Rev Fluid Mech*. 1988;20(1):111–157.

38. Bolintineanu DS, Grest GS, Lechman JB, Pierce F, Plimpton SJ, Schunk PR. Particle dynamics modeling methods for colloid suspensions. *Comput Part Mech*. 2014;1(3):321–356.

39. Witten TA, Sander LM. Diffusion-limited aggregation, a kinetic critical phenomenon. *Phys Rev Lett*. 1981;47(19):1400–1403.

40. Meakin P. Formation of fractal clusters and networks by irreversible diffusion-limited aggregation. *Phys Rev Lett*. 1983;51(13):1119–1122.

41. Kolb M, Botet R, Jullien R. Scaling of kinetically growing clusters. *Phys Rev Lett*. 1983;51(13):1123–1126.

42. Meakin P. Diffusion-controlled flocculation: the effects of attractive and repulsive interactions. *J Chem Phys*. 1983;79(5):2426

43. Meakin P. Diffusion-controlled cluster formation in two, three, and four dimensions. *Phys Rev A*. 1983;27(1):604–607.

44. Meakin P. Diffusion-controlled cluster formation in 2—6-dimensional space. *Phys Rev A*. 1983;27(3):1495–1507.

45. Kolb M, Jullien R. Chemically limited versus diffusion limited aggregation. *J Phys Lettres*. 1984;45(20):977–981.

46. Jullien R, Kolb M. Hierarchical model for chemically limited cluster-cluster aggregation. *J Phys A Math Gen*. 1984;17(12):L639–L643.

47. Meakin P. The effects of random bond breaking on diffusion limited cluster–cluster aggregation. *J Chem Phys*. 1985;83(7):3645

48. Kolb M. Reversible diffusion-limited cluster aggregation. *J Phys A Math Gen*. 1986;19(5):L263–L268.

49. Shih WY, Aksay IA, Kikuchi R. Reversible-growth model: cluster-cluster aggregation with finite binding energies. *Phys Rev A*. 1987;36(10):5015–5019.

50. Shih WY, Liu J, Shih W-H, Aksay IA. Aggregation of colloidal particles with a finite interparticle attraction energy. *J Stat Phys*. 1991;62(5–6):961–984.

51. Haw M. Cluster-cluster gelation with finite bond energy. *Adv Colloid Interface Sci*. 1995;62(1):1–16.

52. Jin J-M, Parbhakar K, Dao LH, Lee KH. Gel formation by reversible cluster-cluster aggregation. *Phys Rev E*. 1996;54(1):997–1000.

53. Terao T, Nakayama T. Sol-gel transition of reversible cluster-cluster aggregations. *Phys Rev E*. 1998;58(3):3490–3494.

54. Gimel JC, Nicolai T, Durand D. Monte-Carlo simulation of transient gel formation and break-up during reversible aggregation. *Eur Phys J E*. 2001;5(4):415–422.

55. Odriozola G, Schmitt A, Moncho-Jordá A, Callejas-Fernández J, Martínez-García R, Leone R, Hidalgo-Álvarez R. Constant bond breakup probability model for reversible aggregation processes. *Phys Rev E*. 2002;65(3):031405

56. Odriozola G, Schmitt A, Callejas-Fernández J, Martínez-García R, Leone R, Hidalgo-Álvarez R. simulated reversible aggregation processes for different interparticle potentials: the cluster aging phenomenon. *J Phys Chem B*. 2003;107(10):2180–2188.

57. Díez Orrite S, Stoll S, Schurtenberger P. Off-lattice Monte Carlo simulations of irreversible and reversible aggregation processes. *Soft Matter*. 2005;1(5):364

58. Babu S, Gimel JC, Nicolai T. Phase separation and percolation of reversibly aggregating spheres with a square-well attraction potential. *J Chem Phys*. 2006;125(18):184512

59. Meakin P, Jullien R. The effects of restructuring on the geometry of clusters formed by diffusion-limited, ballistic, and reaction-limited cluster–cluster aggregation. *J Chem Phys*. 1988;89(1):246

60. van Garderen HF, Dokter WH, Beelen TPM, van Santen RA, Pantos E, Michels MAJ, Hilbers PAJ. Volume fraction dependence and reorganization in cluster–cluster aggregation processes. *J Chem Phys*. 1995;102(1):480

61. Jullien R, Hasmy A. Fluctuating bond aggregation: a model for chemical gel formation. *Phys Rev Lett*. 1995;74(20):4003–4006.

62. Seager CR, Mason TG. Slippery diffusion-limited aggregation. *Phys Rev E*. 2007;75(1):011406

63. Babu S, Gimel JC, Nicolai T. Diffusion limited cluster aggregation with irreversible slippery bonds. *Eur Phys J E*. 2008;27(3):297–308.

64. Aubert C, Cannell DS. Restructuring of colloidal silica aggregates. *Phys Rev Lett*. 1986;56(7):738–741.

65. Cipelletti L, Manley S, Ball RC, Weitz DA. Universal aging features in the restructuring of fractal colloidal gels. *Phys Rev Lett*. 2000;84(10):2275–2278.

66. Dietler G, Aubert C, Cannell DS, Wiltzius P. Gelation of colloidal silica. *Phys Rev Lett*. 1986;57(24):3117–3120.

67. Dimon P, Sinha SK, Weitz DA, Safinya CR, Smith GS, Varady WA, Lindsay HM. Structure of aggregated gold colloids. *Phys Rev Lett*. 1986;57(5):595–598.

68. Kantor Y, Witten TA. Mechanical stability of tenuous objects. *J Phys Lettres*. 1984;45(13):675–679.

69. Liu J, Shih WY, Sarikaya M, Aksay IA. Fractal colloidal aggregates with finite interparticle interactions: energy dependence of the fractal dimension. *Phys Rev A*. 1990;41(6):3206–3213.

70. Parkinson J, Kadler KE, Brass A. Self-assembly of rodlike particles in two dimensions: a simple model for collagen fibrillogenesis. *Phys Rev E*. 1994;50(4):2963–2966.

71. Parkinson J, Kadler KE, Brass A. Simple physical model of collagen fibrillogenesis based on diffusion limited aggregation. *J Mol Biol*. 1995;247(4):823–831.

72. Rothenbuhler JR, Huang J-R, DiDonna BA, Levine AJ, Mason TG. Mesoscale structure of diffusion-limited aggregates of colloidal rods and disks. *Soft Matter*. 2009;5(19):3639

73. McAllister MJ, Li J-L, Adamson DH, Schniepp HC, Abdala AA, Liu J, Herrera-Alonso M, Milius DL, Car R, Prud'homme RK, Aksay IA. Single sheet functionalized graphene by oxidation and thermal expansion of graphite. *Chem Mater*. 2007;19(18):4396–4404.

74. Russel WB, Saville DA, Schowalter WR. *Colloidal Dispersions*. Cambridge: Cambridge University Press, 1992.

75. Mahanty J, Ninham BW. *Dispersion Forces*. London; New York: Academic Press, 1976.

76. Hamaker HC. The London—van der Waals attraction between spherical particles. *Physica*. 1937;4(10):1058–1072.

77. Mer VKL. Nucleation in phase transitions. *Ind Eng Chem*. 1952;44(6):1270–1277.

78. González AE. Colloidal aggregation with sedimentation: computer simulations. *Phys Rev Lett*. 2001;86(7):1243–1246.

79. Lee MH, Furst EM. Formation and evolution of sediment layers in an aggregating colloidal suspension. *Phys Rev E*. 2006;74(3):031401.

80. Poon WCK, Haw MD. Mesoscopic structure formation in colloidal aggregation and gelation. *Adv Colloid Interface Sci*. 1997;73:71–126.

81. Kim JM, Fang J, Eberle APR, Castañeda-Priego R, Wagner NJ. Gel transition in adhesive hard-sphere colloidal dispersions: the role of gravitational effects. *Phys Rev Lett*. 2013;110(20):208302

82. Schniepp HC, Kudin KN, Li J-L, Prud'homme RK, Car R, Saville DA, Aksay IA. Bending properties of single functionalized graphene sheets probed by atomic force microscopy. *ACS Nano*. 2008;2(12):2577–2584.